ITN-5VC

Integrated Telematics for Next Generation 5G Vehicular Communications

ITN-5VC D1.3

Report on phased array MIMO antenna prototype and characterization

Version v1.1 Date: 2024/09/30

Document properties:

Grant Number:	955629
Document Number:	D1.3
Document Title:	Report on phased array MIMO antenna prototype and characterization
Partners involved:	University of Twente, Gapwaves
Authors:	Reza Gheybi Zarnagh, Coen van de Ven, and Andrés Alayón Glazunov (Editor)
Contractual Date of Delivery:	2024/09/30
Dissemination level:	PU[1]
Version:	1.1
File Name:	ITN-5VC D1.3_v1.1

[1] CO = Confidential, only members of the consortium (including the Commission Services)
PU = Public

Table of Contents

Executive summary

This deliverable provides a comprehensive report on the development and characterization of mmWave antenna prototypes, created as part of WP1 in the ITN-5VC project. The primary goal of these prototypes is to assess and enhance the performance of cutting-edge array antennas at mmWave frequencies for joint communication and sensing (JCAS) systems, as well as automotive radar applications. This report represents a collaborative effort between ESR 1 and ESR 3, focusing on the design of mmWave antennas tailored for both applications. It includes detailed simulation results from electromagnetic analyses and empirical data obtained from measurements of the fabricated array antenna prototypes.

List of Figures

List of tables

List of acronyms and abbreviations

EM	Electromagnetic
ESR	Early-Stage Researcher
FoV	Field of View
GW	Gap Waveguide
GRIN	Gradient index
HPBW	Half Power Beamwidth
JCAS	Joint Communication and Sensing
MLW	Multi-Layer Waveguide
mmWave	Millimetre Wave
PCB	Printed Circuit Board
SLL	Side Lobe Levels
UT	University of Twente
WP1	Work Package 1

1 Introduction

For the Joint Communication and Sensing (JCAS) system developed in ITN-5VC, work package 1 (WP1) focuses on the design and characterization of millimetre-Wave (mmWave) phased array antennas. This deliverable reports on the design results of the array antenna prototypes created by ESR 1 and ESR 3. These results consist of simulation results using full-wave simulations as well as measurements performed on the manufactured prototypes. These aid the channel models created by ESR 4, to create a model of the propagation environment of the hyperconnected car proposed in the project.

The design and characterization of the mmWave array antenna prototypes are divided into two main categories. The first category focuses on the array antenna for automotive radar. For this array antenna, the frequency band of 76 to 81 GHz has been chosen due to the large available bandwidth. This large bandwidth offers better range resolution than the 24 GHz band, which is being phased out for automotive radar. Additionally, this frequency band does not suffer as much from the increased path loss found at higher frequencies, such as the available bands around 140 GHz. The second category focuses on an array antenna for JCAS. For this application, the same frequency range is used, as the large bandwidth offers a similar advantage for sensing accuracy as well as a potential for high data rates.

2 Automotive radar array antenna

At the frequency range of interest, it is well known that waveguide-based antennas offer low loss and high aperture efficiency compared to PCB-based technologies such as microstrip antennas and substrate-integrated waveguides. Using gap waveguide (GW) technology, designs can be created which are suitable for large-volume production. This technology uses a planar stack of different layers, allowing for efficient integration with the active circuits on the PCB and allowing for the use of planar array for the purpose of angular detection. For our protypes we have focussed on corner and medium-range radar, the relevant specifications can be found in Table 1.

Table 1. Specification of two different types of automotive radar

Specification	Corner Radar	Medium range radar
Return loss	-10 dB	-10 dB
Azimuth Field of view	120 degrees HPBW	50 degrees HPBW
Elevation Field of view	25 degrees HPBW	25 degrees HPBW
Frequency Range	76-81 GHz	76-81 GHz
Sidelobe level	-20 dB	-20 dB

2.1 Array antenna design

For the antenna design, the Multi-Layer waveguide (MLW) technology has been chosen, which is the latest improvement to the traditional GW technology. This is due to the small formfactor as well as it's suitability for high volume production. Moreover, the MLW technology offers similar low losses compared to PCB-based technologies and a high aperture efficiency like other waveguide-based solutions. Fig. 1 shows the designed antenna element in MLW technology

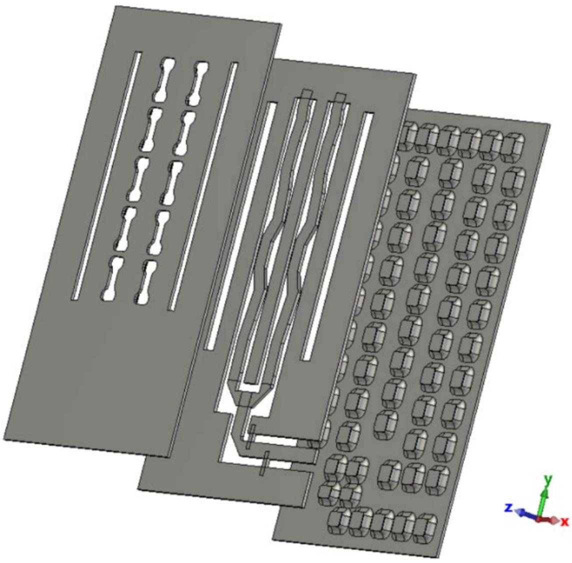

Fig. 1. Antenna element design in Multi-Layer Waveguide (MLW) technology

The array antenna design consists of two columns of 5 slots to achieve the targeted specification for a medium-range radar as stated in Table 1. This antenna element is designed using full-wave simulations, where the return loss and radiation patterns have been evaluated; these results are shown in Fig. 2 and Fig. 3, respectively.

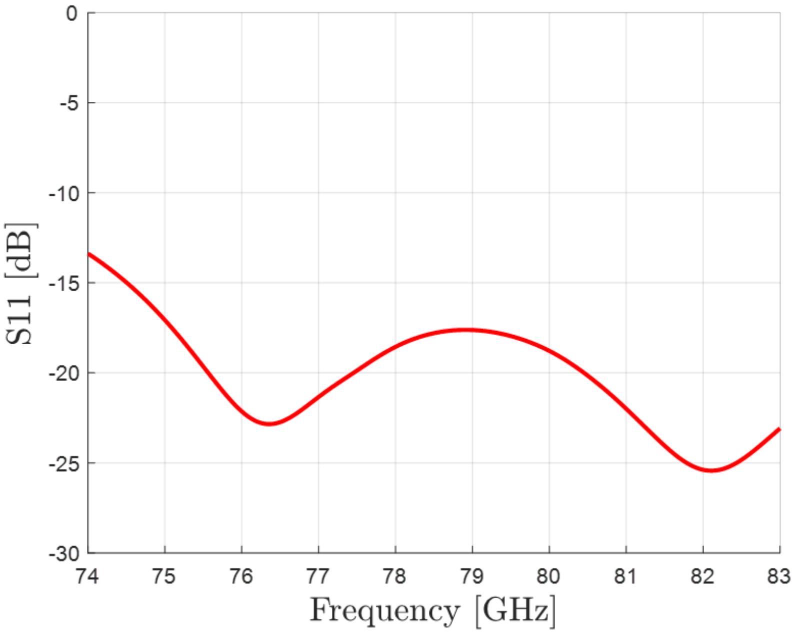

Fig. 2. Return loss of the antenna element

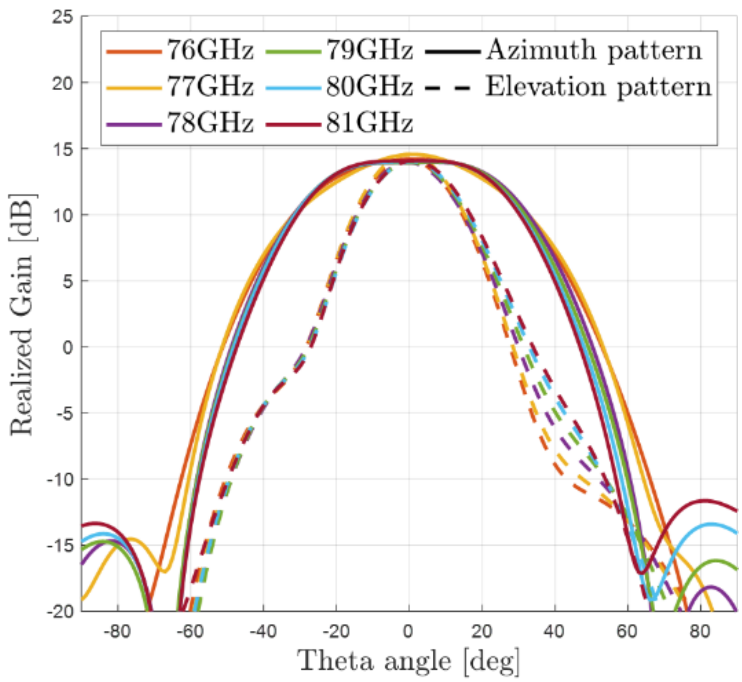

Fig. 3. Radiation patterns of the antenna element

As seen in Fig. 2, the return loss is below the required -10 dB across the entire frequency band. This margin is necessary because the return loss is expected to increase when more components are added to complete the full array antenna design. Regarding the far-field results shown in Fig.

3, the radiation pattern remains stable over the entire frequency range, and the antenna element meets the specification on HPBW and SLL.

2.2 Gradient index lensing

To enhance the performance of automotive radar, it is beneficial to shape the radiation pattern of the antenna elements. Traditionally, this is achieved through antenna design, where several techniques can be used. A few examples include adding parasitic elements such as corrugations, or chokes, introducing EBG structures, adding so-called 'dummy' antennas or shaping the aperture into a horn. One technique that has attracted significant attention in recent years is metamaterial lenses. In one of the earlier works of the project [1], a similar method was demonstrated, allowing us to shape the radiation pattern with lensing features. In this work, we were able to demonstrate that it is possible to reduce the size of such lenses to fit within the spacing of automotive array antennas [2]. Although we were not able to validate this method before using a fabricated lens, such validation is planned for an upcoming conference paper for EUCap2025. For this deliverable, we have demonstrated that such features can be integrated inside a Radome, which is crucial to bring this solution to the market.

Similar to the lens designed in [2], the proposed solution uses a gradient index (GRIN) lens to shape the radiation pattern. Fig. 4 shows the unit cell of this gradient index material. In this unit cell, the dielectric constant can be changed by changing the ratio between c_y and p_y.

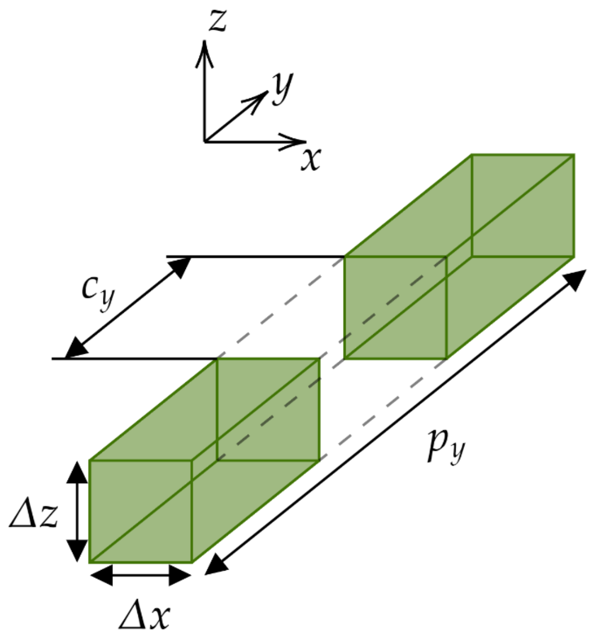

Fig. 4. Unit cell of the gradient index lens

The effective dielectric constant ϵ_{eff} of the material can be changed throughout the lens following the relation [3]:

$$\epsilon_{eff} = \epsilon_r - \frac{c_y}{p_y}(\epsilon_r - \epsilon_0), \quad (1)$$

where $\epsilon_r = 2.53$ is the dielectric constant of the plastic material chosen for the lens, ϵ_0=1 is the background dielectric constant. By changing the effective dielectric constant throughout the design of the lens, a gradient is created which controls the propagation of the EM wave, hence the name Gradient index (GRIN) lensing. The designing of the lens aims to achieve the radiation pattern for the corner radar with parameters given in Table 1. The simulated radiation pattern of the designed GRIN lens is shown in Fig. 5, where the simulated radiation pattern of the antenna without the lens is added in the figure.

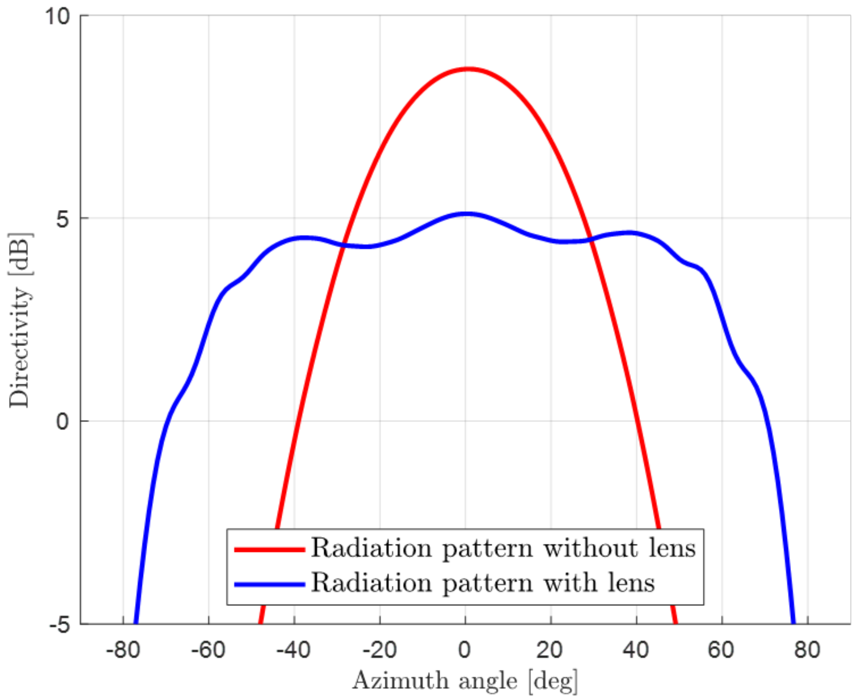

Fig. 5. Radiation pattern results of the unit cell design.

2.3 Characterization of the automotive array antenna

To demonstrate the approach outlined above, two radomes were designed. One of the radomes is a standard radome of a half-wavelength thickness, and the other implements a GRIN lens. Fig. 6 shows the designed prototype. The layout of the antenna elements has been inherited from a corner radar design [4], ensuring that all limitations related to the feeding of the elements, as well as all the mechanical and manufacturing constraints seen in automotive antenna design. The design of this array antenna together with the two Radomes are the main results which will be further elaborated in a journal paper, which is being finalized at the time of this deliverable. Within this journal paper we will elaborate on the method and design of the integrated GRIN lens and will be called “Integrated GRIN Lens in Radome for mmWave Automotive Radar”.

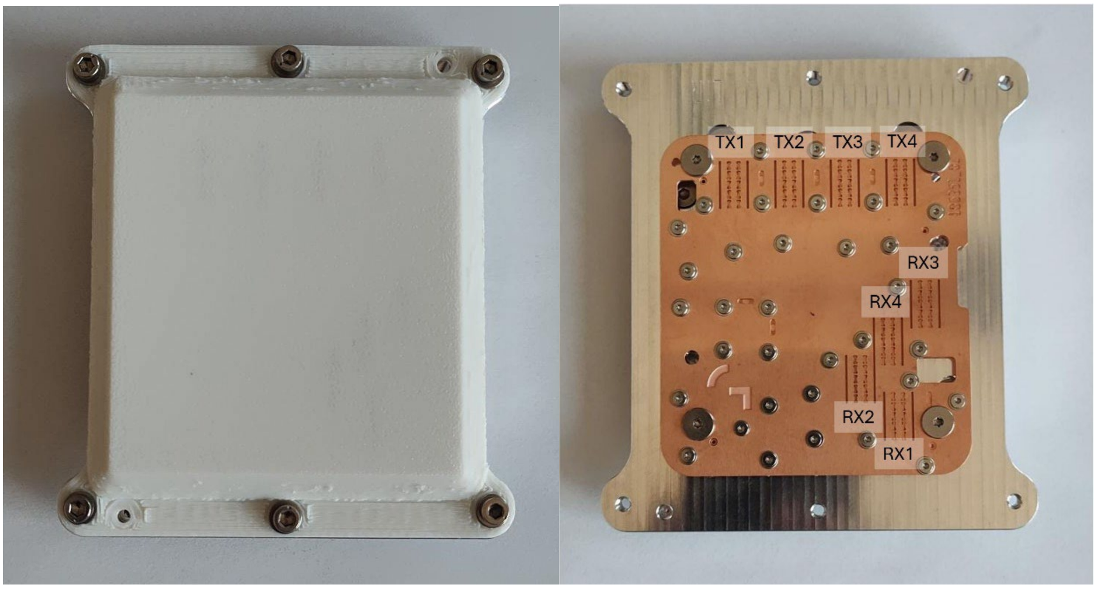

Fig. 6. Pictures of the manufactured array antenna prototype with and without radome

As mentioned earlier, the purpose of the radome is to shape the radiation pattern of the antenna element. As part of the initial characterization of the array antenna prototypes as well as the ability the shape the radiation pattern using our GRIN lens, farfield measurements have been performed in the anechoic chamber at Gapwaves AB. Fig. 7 shows the anechoic chamber and the measurement setup which was used.

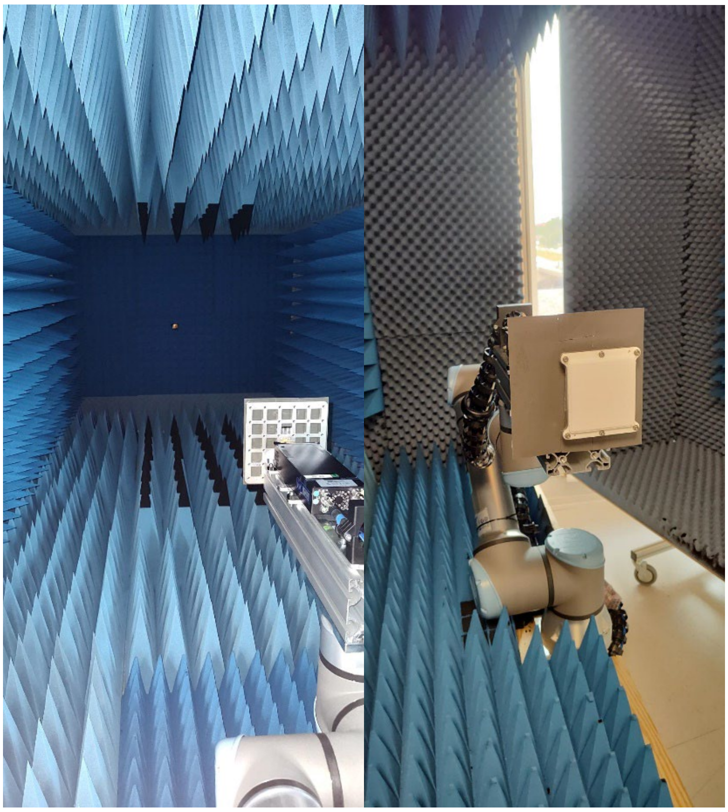

Fig. 7. Anechoic chamber measurement setup at Gapwaves AB

From these measurements the radiation pattern of all eight channels of the array antenna have been measured with both radomes, these results are shown in Fig. 8. As can be seen, the radome successfully shaped the radiation pattern, increasing the beamwidth of the antenna element.

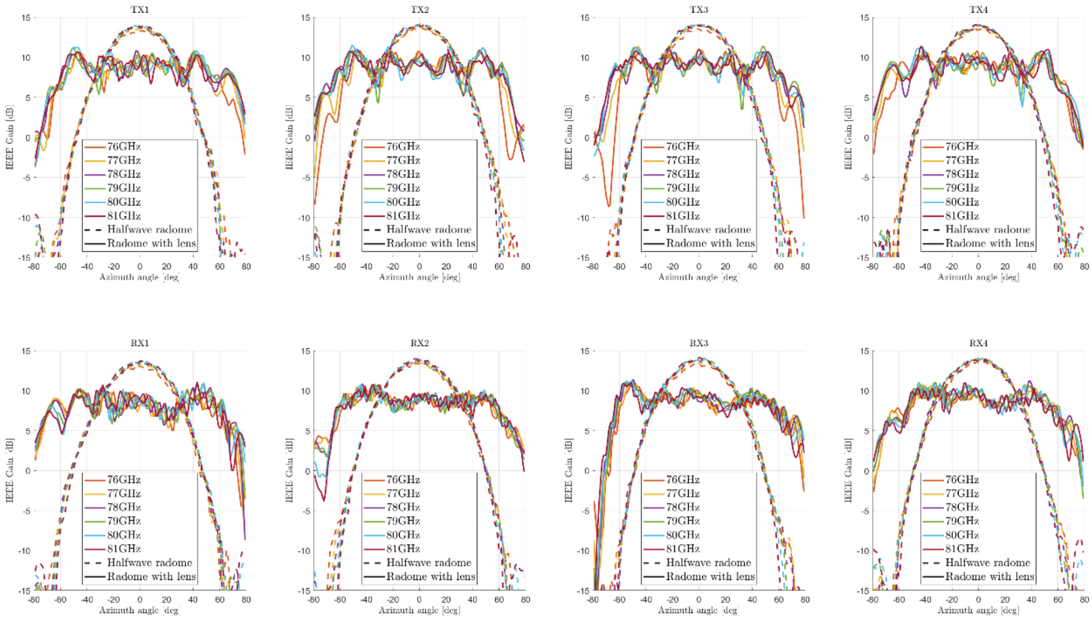

Fig. 8. Measured radiation patterns of the array antenna with two different radomes

Besides the radiation pattern, the return loss is also an important figure of merit for array antennas. Fig 9 shows the return loss for all ports of the array antenna, measured using a VNA. Unfortunately, a manufacturing error occurred, which primarily impacted the return loss, as shown in Fig 10. To evaluate the impact of this error, it was included in the simulations. The nominal return loss is below the specification set for the array antenna. Despite the increased return loss due to the manufacturing issue, most channels demonstrate a return loss below -10 dB for most of the frequency band of interest.

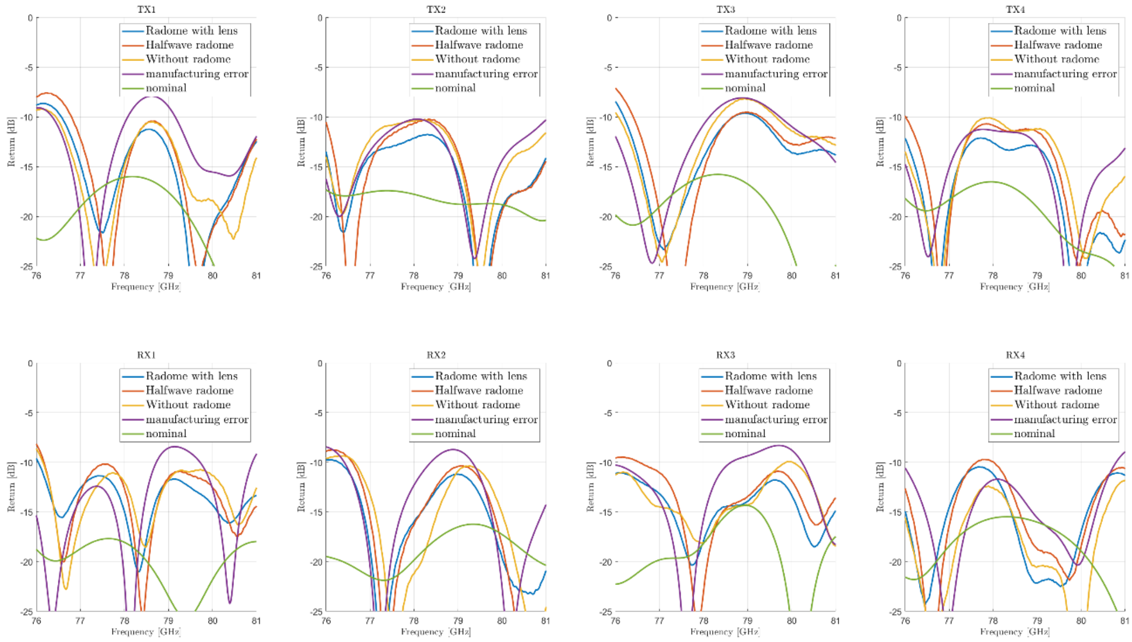

Fig. 9. Measured return loss of the manufactured array antennas together with simulation results of the nominal design and the design including the found manufacturing error.

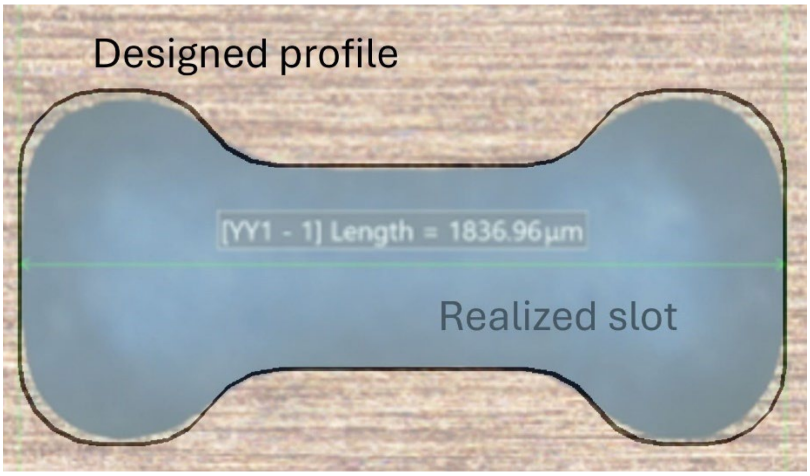

Fig. 10. Changed profile of the radiating slots due to a manufacturing error

2.3.1 RLOS environment

The Random Line-of-sight (RLOS) environment testing methodology (e.g. see D1.1 and D1.2) evaluates the cumulative distribution functions (CDF) as an important performance metric. In Fig. 11, the CDF of the azimuth pattern is shown of the array antenna with the two different radomes. There is a cross over around 0.6 which would indicate that the Radome with lens offers higher Gain for 60% of random Line of sight channels. The Halfwave Radome offers higher peak gain, however for randomly positioned targets there is a higher probability that the channel gain is much lower. Hence, statistically speaking, the Radome with lens provides a more uniform coverage of signals arriving over a wider FoV of the antenna. This further demonstrates the superior performance of the Radome lens for radar applications.

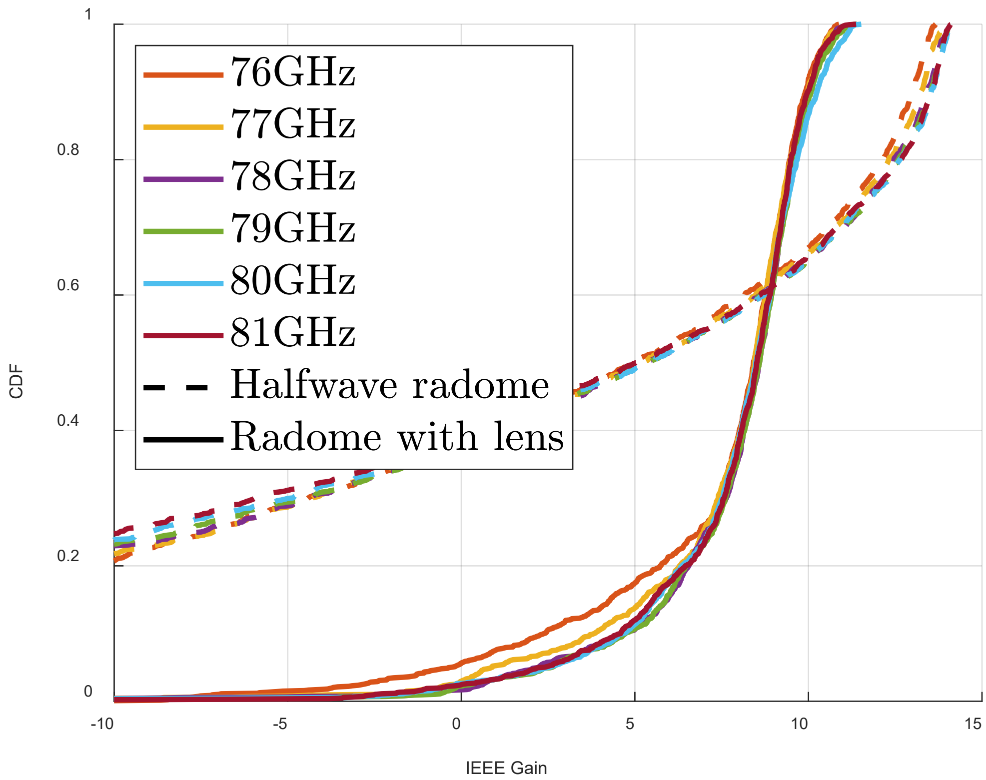

Fig. 11. Cumulative Distribution Function of the automotive array antenna

2.3.2 RIMP environment

As mentioned in D1.1. and D1.2, for the evaluation in the RIMP environment, one the most relevant figures of merit is the Total Radiated Power (TRP). Here we present TRP results based both on simulation and obtained from measurements in the anechoic chamber. The TRP is computed as follows

$$TRP = \int_0^{2\pi} \int_0^{\pi} U(\theta, \phi) \sin(\theta)\, d\theta d\phi \,, \qquad (2)$$

where $U(\theta, \phi)$ is the radiation intensity and θ and ϕ are the elevation and azimuth spherical angles, respectively.

The radiation efficiency is related to the antenna Gain $G(\theta, \phi)$ is via

$$G(\theta, \phi) = \frac{4\, \pi U(\theta,\phi)}{P_t}, \qquad (3)$$

Where P_t it the transmit Power fed to the antenna, which is taken as 1W. Altough the facility of the measurement chamber allows for a large scanning range in the two main planes, the angular range to perfrom spherical measurements is limited to ±70 degrees in azimuth and ±50 degrees in elevation. The values of the radiation intensity at angles outside the angular range of the measurement setup are set to zero, which allows us to compute the integral in (2) despite the limitation of the anechoic chamber. Fig. 12 shows the measured Gain of the automotive array antenna using the two different radomes.

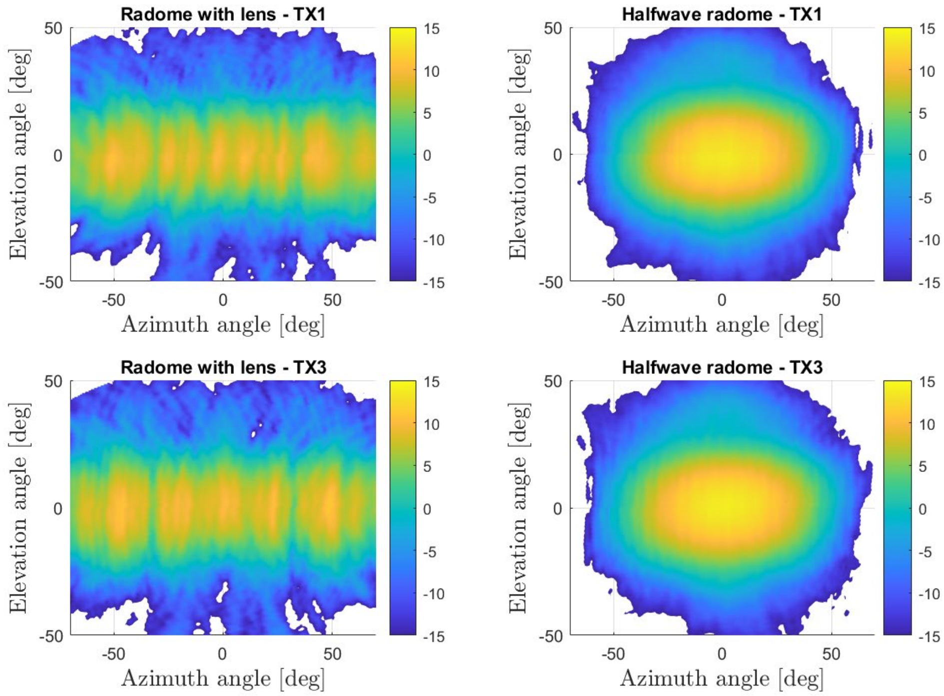

Fig. 12. measured Gain of the Automotive array antennas

The TRP shown in Fig. 13 was obtained from calibrated measurement data. Since were not able to capture the full sphere, we have also computed the TRP using full wave simulations which is shown in Fig. 14.

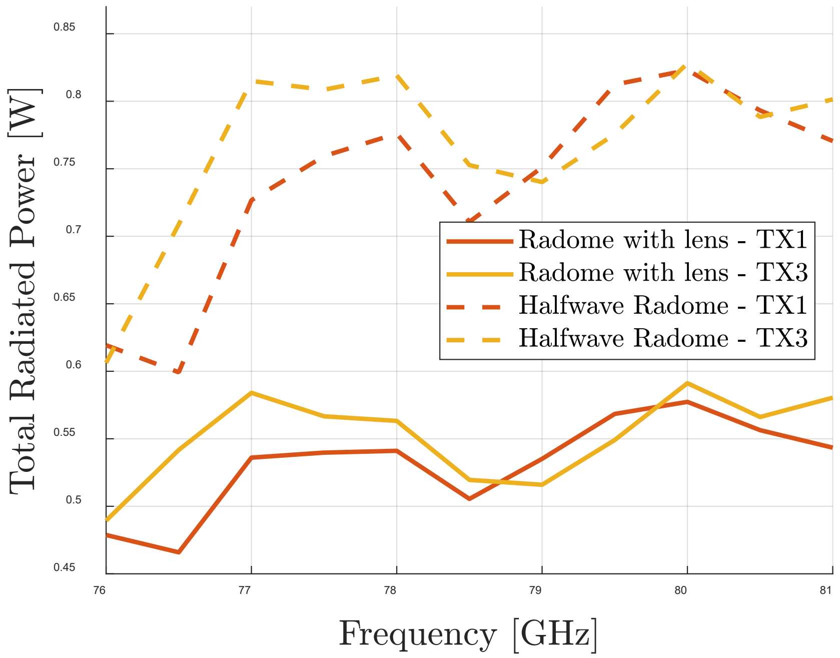

Fig. 13. Total Radiated Power calculated from the anechoic measurement

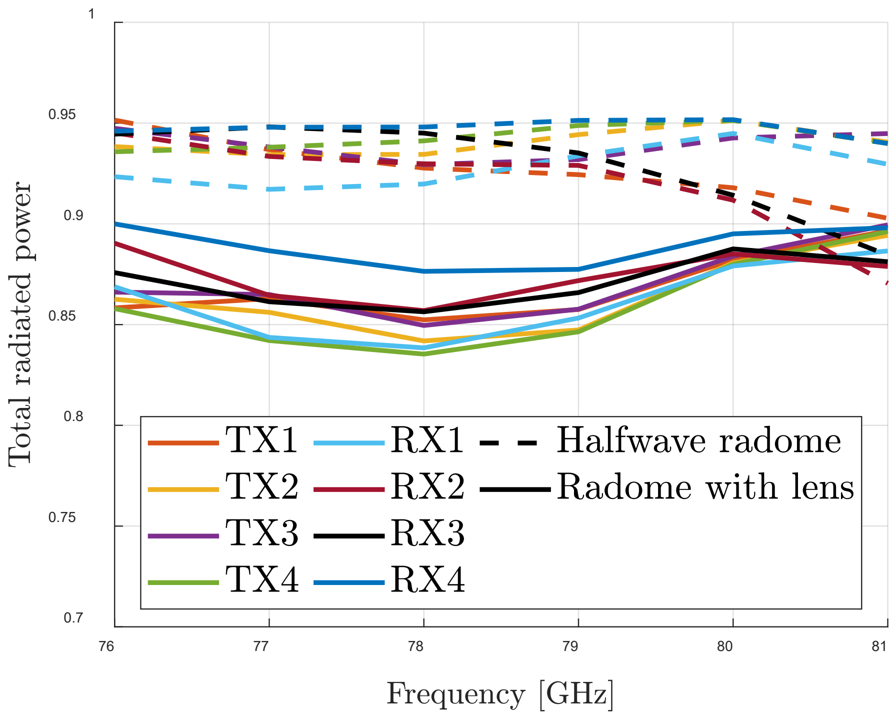

Fig. 14. Total Radiated Power computed from full-wave simulations

As can be seen from both methods, the TRP is lower for the Radome with integrated lens compared to the halfwave Radome. This is most likely due to the increased excitation of propagating modes in the ticker Radome where the lens is integrated. Furthermore, from the measurement results In Fig. 13 it can be seen that the TRP for both radomes is lower than the results from the simulation in Fig. 14. Part of the reason is that we have had to remove the ohmic losses in the full wave simulation to reduce the simulation time. Additionally, we were not able to measure the full sphere, which also reduces the computed TRP, since the values outside of the spherical range which can be measured are set to zero. Especially for the measurement with the integrated lens in the Radome, a not insignificant part of the power radiates beyond the angular limits of the measurement setup. This can be seen from the measured Gain at ±70 degrees in azimuth in Fig. 12.

3 Gap Waveguide Array Antenna for Joint Communication and Sensing Systems

Most research efforts on JCAS systems have primarily focused on single-beam transmitter and receiver antennas, which may limit the sensing direction to align with the communication direction. Recent studies have suggested using simultaneous, distinguishable beams for communication and sensing separately [5]. A major challenge that may arise in JCAS systems is the coupling of the transmit (TX) antenna and the receive (RX) antenna signal paths, as well as potential interference between the radar and communication radiation patterns of the antennas [6]. Several techniques at system level have been developed to enhance the isolation between the communication and sensing components. However, in terms of hardware, polarization diversity can be an effective solution to reduce self-interference in antennas. Employing orthogonally polarized antennas is a well-known technique to increase the capacity and reliability of wireless systems.

The mmWave frequency range provides a great opportunity to integrate communication and sensing functions into a single, jointly designed system, thanks to its wide available bandwidth and the possibility to design low-profile antennas.

In mm-Wave frequency bands, Gap Waveguide technology provides a strong foundation to take advantage of the wide available bandwidth. This technology overcomes the issues related to dielectric and transmission losses, ensuring a high-gain solution by creating a PEC/PMC stopband for parallel-plate modes and confining electromagnetic wave propagation within the guiding structure.

In the proposed antenna, a new technique based on gap waveguide technology has been devised to achieve vertical polarization. The vertically polarized antenna, alongside the traditional horizontally polarized gap waveguide antennas, can serve as a suitable complement to create a jointly designed communication and sensing system with improved isolation between antenna components. The following section will describe the design process of the vertically polarized array antenna and optimized simulation results.

3.1 Array antenna design

The proposed array antenna consists of 8 subarrays, each subarray in turn consists of 8 radiating, horizontally arranged linear slots. The entire antenna consists of 4 layers, which from bottom to top are defined as: the distribution layer, first transition layer, second transition layer, and the radiating layer. In the distribution layer, H-holes are employed in the middle of each subarray to feed the entire subarray through two parallel ridges. As shown in Fig. 15, the second layer consists of 4 up/down arranged V-shape slots with an inter-element spacing of λ_g. λ_g is the guided wavelength of the EM-mode propagating in the ridge waveguide created in the distribution layer. The surrounding of each V-shape slot is λ_g, and they are devised to configure vertical polarization. The second layer also contains 4 cavities that act as a transition element to upper layers. To achieve good impedance matching, two opposite edges of each cavity are tapered into bow-tie-shaped elements. Metallic pins surround each cavity to create a stop band suppressing the leakage waves. The third layer complements the second transition layer by equally dividing the power of the EM waves and coupling them to the radiating slots. Finally, the top layer is the radiating layer, which includes 8 horizontally arranged linear slots that produce vertical polarization. It is noteworthy mentioning that each cavity directly feeds two horizontal slots spaced by $\lambda_g/2$. In this way, the lobes that could arise from the larger inter-element spacing of V-shaped slots are compensated. Due to the close positioning of the slots in the azimuth direction, unavoidable coupling between them can affect the performance of the antenna. Optimized metallic walls located on the radiating layer help reducing the coupling between slots.

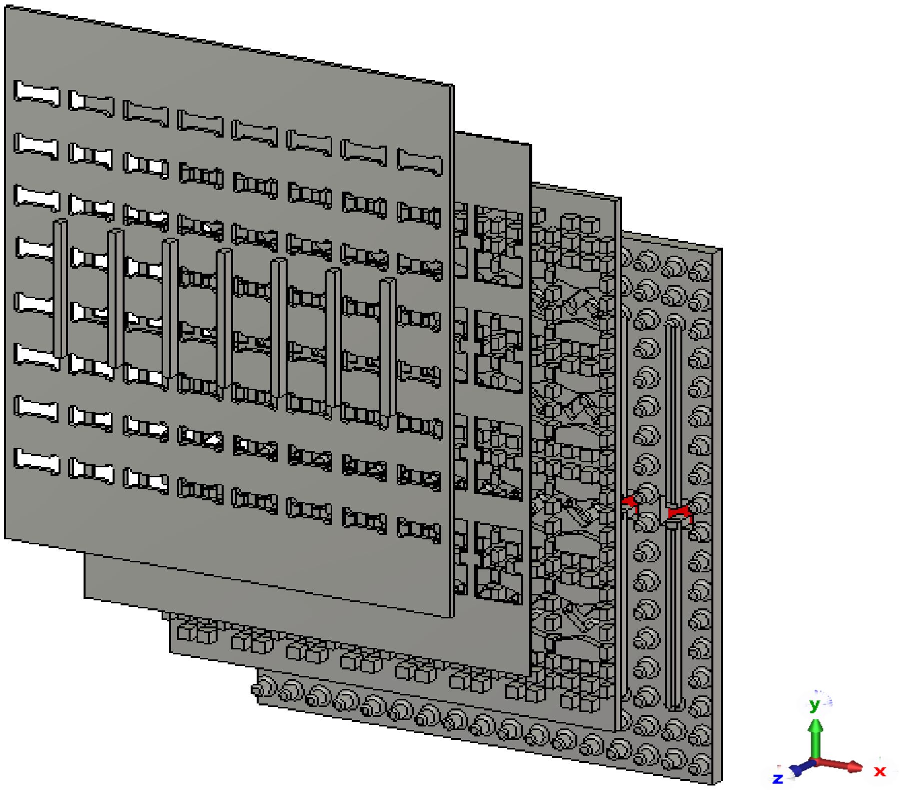

Fig. 15. Perspective view of the vertically polarized array antenna.

3.2 Simulation Results

The following sections present the simulation results for the vertically polarized array antenna. The proposed array antenna was simulated and optimized using CST Microwave Studio software.

3.2.1 Electric field distribution

As can be seen from Fig. 16(a), which shows the electric field distribution in the V-shaped slot, the electric field arrows are perpendicular to the side walls of the slot. The superposition of these electric fields creates a total field in the longitudinal direction of the ridge, which in turn produces vertical polarization. However, due to the spacing between the slots of λ_g, grating lobes appear in the elevation plane. To mitigate the issue of high grating lobe levels, horizontally arranged slots have been implemented, consisting of 8 transverse slots with an inter-element spacing of $\lambda_g/2$, as shown in Fig. 16(b). It can also be seen from the same figure that the electric field arrows are perpendicular to the large walls of the slots and tangent to the direction of the ridge.

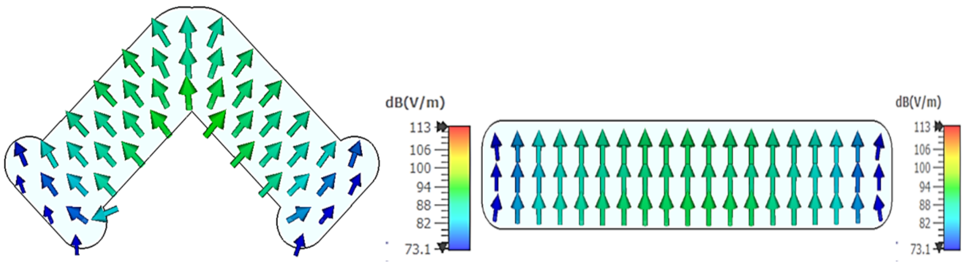

(a) (b)

Fig. 16. Field distribution of the slots (a) V-shaped slot and (b) transverse slot.

3.2.2 Return loss

This section presents the simulated embedded reflection coefficients for the designed array antenna. As shown in Fig. 17, the antenna covers the frequency band from 76 − 81 GHz. This band is allocated to the automotive radar applications; however, the designed antenna can be effectively used for both communication and radar applications. Moreover, as shown in Fig. 17, a good impedance matching between the distribution layer and top layers has been achieved. Due to the asymmetric structure of the antenna, caused by the presence of metallic walls on the radiating layer, the edge ports see different impedances, which leads to slightly different S-parameter results.

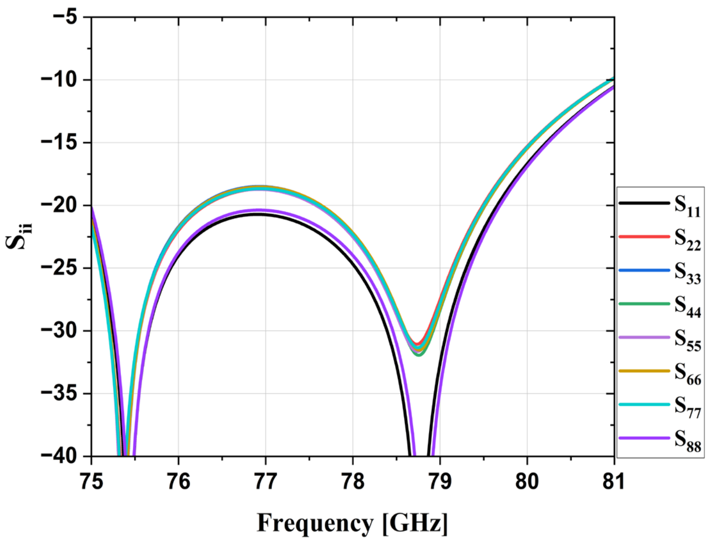

Fig. 17. Simulated embedded Reflection Coefficients.

3.2.3 Radiation patterns

The simulated radiation patterns of the array antenna in the azimuthal and elevation plane are depicted in Fig. 18. The antenna with 8×8 radiating elements achieves a peak realized gain of

20.9 dBi, with sidelobe levels (SLL) of –13.7 dB in the E-plane and –12.8 dB in the H-plane. This realized gain is achieved by exciting the 8 elements (each consisting of 8 slots) and beamforming toward the broadside direction.

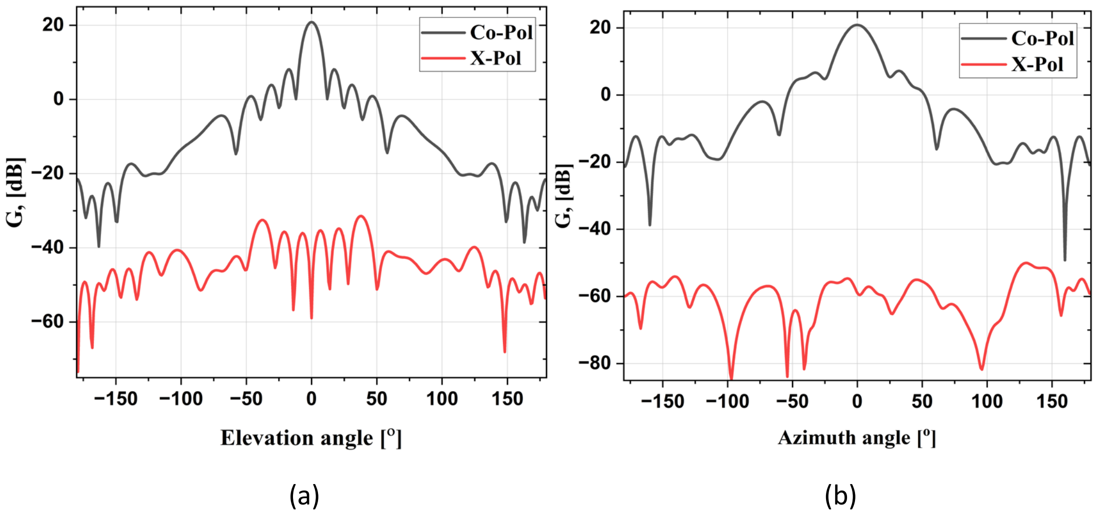

Fig. 18. Co-polarized and X-polarized simulated patterns of the antenna at 77 GHz (a) E-plane and (b) H-plane.

3.2.4 Scanning capability

The scanning performance of the array antenna in the azimuth plane is shown in Fig. 19. The scanning angles cover a ±40° field of view. Due to the transverse arrangement of the slots, the inter-element spacing exceeds $\lambda_g/2$. However, all the cavities and the intervening pins are carefully tuned to ensure the slots are positioned at the correct distances from each other.

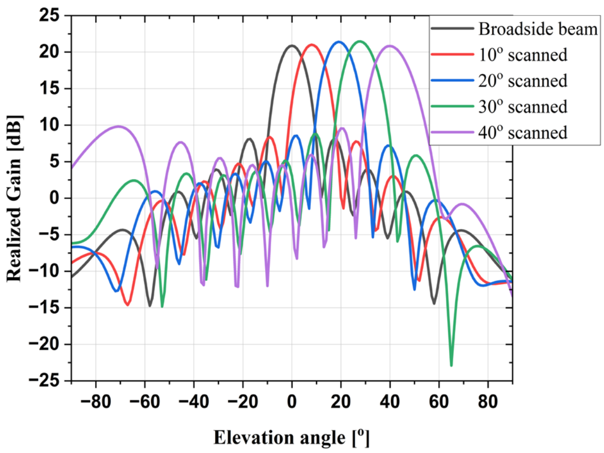

Fig. 19. Azimuth scanning at 10° step at 77 GHz.

3.2.5 Random Line of Sight (RLOS) environment evaluation

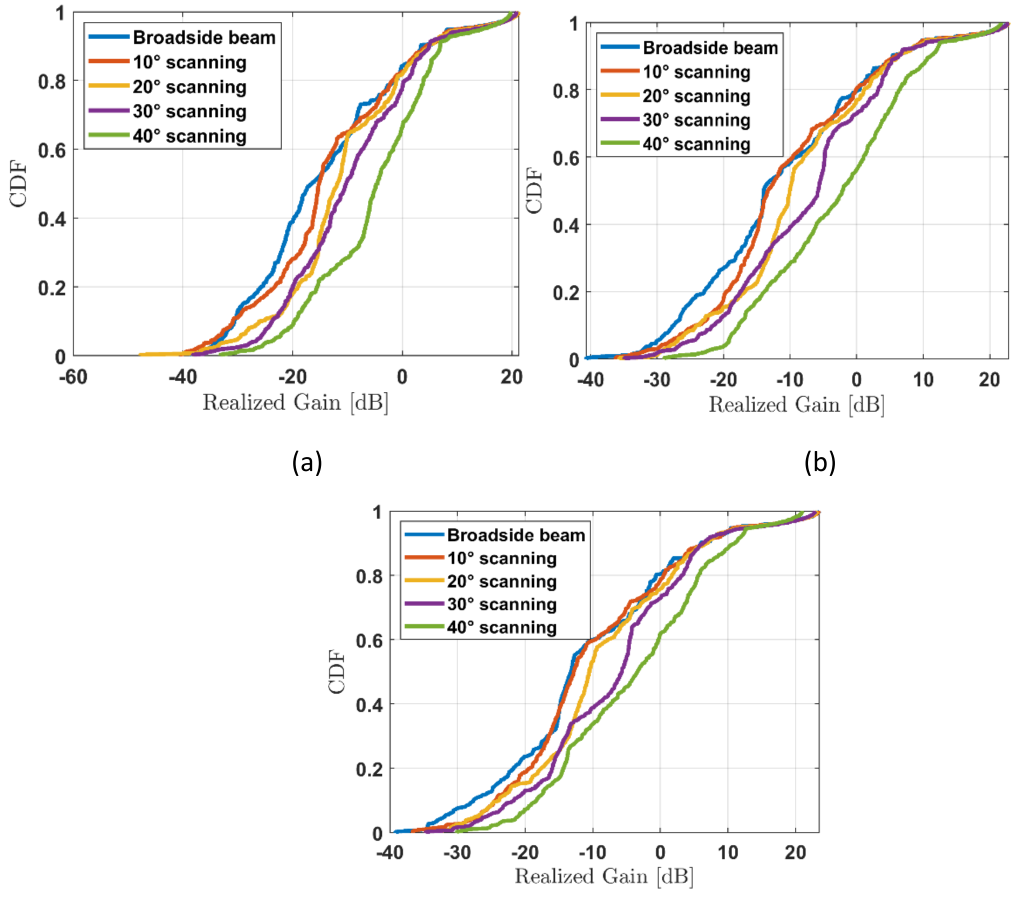

(a) (b)

(c)

Fig. 20. Cumulative Distribution Function of the array antenna at a) 76 GHz, b) 79 GHz, c) 81 GHz.

To evaluate the performance of the antenna in random line-of-sight (RLOS) environments, the Cumulative Distribution Function (CDF) of the azimuth radiation pattern of the array antenna is shown in Fig. 20. The figure represents the CDFs of scanning beams at 0, 10, 20, 30 and 40 degrees and at three frequencies, i.e., 76 GHz, 79 GHz, and 81 GHz. It is obvious that at three frequencies, half of the sphere is covered with the required power. The shifting of the curves to the right as the scanning angle increases shows the widening of the main beam. A maximum beam gain is consistently maintained with frequency and the considered beam scanning angles, with a minor scanning loss at 40-degree scanning. This shows the consistently high performance of the antenna.

3.2.6 Rich Isotropic Multi-Path (RIMP) environment evaluation

To evaluate the performance of the antenna in the RIMP environment, the total radiated power of the antenna in the full sphere has been presented in Fig. 21. The TRP values for 1 W input power have been computed using the equation (2) and integrating over the whole sphere. The results have been shown for the broadside beam and the scanned beams, i.e., the beams at 0, 10, 20, 30, and 40 degrees, indicate that at higher frequencies there is a drop in the TRP which refers to the return loss of the antenna with low impedance matching at higher frequencies. Also, for the scanned beams, the active reflection loss is not as good as the broadside beam, consequently impacting the TRP with a drop in its value.

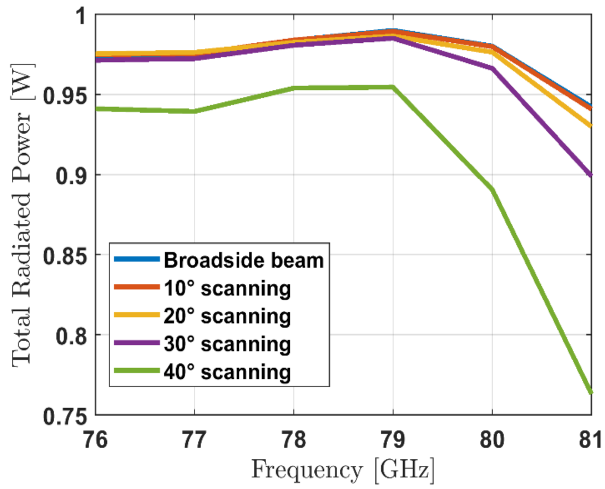

Fig. 21. Total Radiated Power of the array antenna.

3.3 Discussion

According to the objectives of the ITN-5VC project for ESR1, an array antenna based on the gap waveguide technology has been designed for joint communication and sensing systems. The antenna with the ability to produce vertical polarization is a proper candidate to use in JC&S systems which offer polarization diversity to cancel the self-interference. The antenna itself offers a wide bandwidth covering the radar band which can be used for both communication and sensing functions. To evaluate the performance of the antenna in RLOS and RIMP environments, two CDF and TRP figures of merit have been characterized which indicate the good performance of the antenna in such environments. Moreover, to reach the objectives, in [7], a dual-linear polarized antenna has been proposed. The antenna produces dual-slant polarizations and has been intended to be used in JC&S systems that improve the isolation between their parts. In [8], a vertically polarized subarray antenna is designed for JC&S systems.

Finally, in [9], the correlation and non-orthogonality figures of merit of beamforming fields of adjacently placed array antennas have been characterized when the beams of antennas pointing different directions. It is shown that in RLOS and RIMP environments, there are different values for correlation and non-orthogonality when the beamforming fields pointing in the same direction or in different directions.

The simulation results have been aligned with project objectives and with the previously published related deliverables i.e., Deliverable 1.1 and Deliverable 1.2.

4 Conclusions

In this deliverable, we showcase the cutting-edge design and characterization of a mmWave array antenna. Our innovative designs, crafted using multi-layer waveguide (MLW) and gap waveguide (GW) technologies, are engineered for high-volume production and are ideally suited for the automotive market. We present detailed simulation results alongside measurement data from our manufactured prototypes, demonstrating the antenna's performance.

The results shown automotive radar applications, are the main results of the work from ESR 3 within the ITN-5VC project. Together with the electromagnetic models which were created for D1.1, novel components have been developed to enhance the performance of automotive phased array antennas on system level. These components are used to develop an array antenna tailored for medium-range radar and introduced a Gradient Index (GRIN) lens to shape the radiation pattern. This advanced method not only adapts the antenna for corner radar applications but also paves the way for enhanced radiation patterns, significantly boosting radar sensor detection capabilities.

The work of ESR 1 has focussed on the development of low-cost and highly efficient phased array antennas together, together with their characterization for joint communications and sensing. To achieve this dual function at mmWave, polarization diversity can be exploited. This can be achieved by using the vertically polarized array antenna which we have presented. Combined with traditional horizontally polarized waveguide antennas, this design leverages polarization diversity to its fullest. This approach enhances the available data rate for communication, enriches target information for sensing, and improves isolation between combined functions within a unified system.

Our work represents a significant leap forward, offering versatile solutions that drive both automotive radar and integrated communication and sensing applications.

References

[1] C. van de Ven, A. Haddadi and A. A. Glazunov, "Automotive RADAR Planar Antenna Optimization Based on Conformal Transformation Optics," 2023 17th European Conference on Antennas and Propagation (EuCAP), Florence, Italy, 2023, pp. 1-5, doi: 10.23919/EuCAP57121.2023.10133336.

[2] C. Van de Ven, A. Haddadi and A. A. Glazunov, "Radiation Pattern Shaping Using Generalized Luneburg Lenses for Automotive RADAR Antennas," 2024 18th European Conference on Antennas and Propagation (EuCAP), Glasgow, United Kingdom, 2024, pp. 1-5, doi: 10.23919/EuCAP60739.2024.10501666.

[3] T. C. Choy, Effective Medium Theory, Oxford, U.K.:Oxford Univ. Press, 2016.

[4] J. -L. A. Lijarcio, A. Vosoogh, C. Bencivenni and A. U. Zaman, "Low-cost Coaxial Slot Array Antenna for E-Band Automotive Corner Radar Applications Based on Gap Waveguide MLW Technology," 2024 18th European Conference on Antennas and Propagation (EuCAP), Glasgow, United Kingdom, 2024, pp. 1-5, doi: 10.23919/EuCAP60739.2024.10501159.

[5] C. B. Barneto, S. D. Liyanaarachchi, T. Riihonen, L. Anttila and M. Valkama, ”Multibeam Design for Joint Communication and Sensing in 5G New Radio Networks,” ICC 2020 - 2020 IEEE International Conference on Communications (ICC), Dublin, Ireland, 2020, pp. 1-6, doi: 10.1109/ICC40277.2020.9148935.

[6] M. Heino, C. Baquero Barneto, T. Riihonen and M. Valkama, ”Design of Phased Array Architectures for Full-Duplex Joint Communications and Sensing,” 2021 15th European Conference on Antennas and Propagation (EuCAP), Dusseldorf, Germany, 2021, pp. 1-5, doi: 10.23919/Eu- CAP51087.2021.9411430.

[7] R. G. Zarnagh, A. Haddadi and A. A. Glazunov, "A Dual Linear-Polarized Gap Waveguide Antenna Element for Radar and Communications at 77 GHz," 2024 18th European Conference on Antennas and Propagation (EuCAP), Glasgow, United Kingdom, 2024, pp. 1-5, doi: 10.23919/EuCAP60739.2024.10501068.

[8] R. G. Zarnagh, A. Haddadi and A. A. Glazunov, "A Dual-Layer Gap Waveguide Antenna with Vertical Polarization for Full-Duplex Joint Communication and Sensing Systems," 2023 IEEE International Symposium On Antennas And Propagation (ISAP), Kuala Lumpur, Malaysia, 2023, pp. 1-2, doi: 10.1109/ISAP57493.2023.10388797.

[9] R. G. Zarnagh and A. Alayón Glazunov, "Correlation and Non-Orthogonality Figures of Merit of Beamforming Fields," 2023 17th European Conference on Antennas and Propagation (EuCAP), Florence, Italy, 2023, pp. 1-5, doi: 10.23919/EuCAP57121.2023.10133475.